

Mode transitions and spoke structures in $E \times B$ Penning discharge

M. Tyushev^{a)},¹ M. Papahn Zadeh,¹ N. S. Chopra,² Y. Raites,² I. Romadanov,²
A. Likhanskii,³ G. Fubiani,⁴ L. Garrigues,⁴ R. Groenewald,⁵ and A. Smolyakov¹

¹⁾*Department of Physics and Engineering Physics, University of Saskatchewan,
Saskatoon SK S7N 5E2, Canada*

²⁾*Princeton Plasma Physics Laboratory, Princeton, New Jersey 08540,
USA*

³⁾*Applied Materials Inc, 35 Dory Rd, Gloucester, MA 01930,
USA*

⁴⁾*LAPLACE, Université de Toulouse, CNRS, INPT, UPS, 118 Route de Narbonne,
31062 Toulouse, France*

⁵⁾*TAE Technologies Inc, 19631 Pauling, Foothill Ranch, CA 92610,
USA*

^{a)} Electronic mail: mikhail.tyushev@usask.ca; Corresponding author

Two-dimensional particle-in-cell simulations in the (radial-azimuthal) plane perpendicular to the axial direction of a cylindrical $\mathbf{E} \times \mathbf{B}$ Penning discharge are presented. The low-pressure discharge is self-consistently supported by plasma ionization from the electron beam injected axially, along the direction of the external magnetic field. It is shown that with the increasing strength of the external magnetic field, the discharge undergoes a sequence of transitions between several azimuthal modes. Azimuthal $m > 1$ spiral arm structures are excited at low magnetic field values as plasma confinement improves and the radial density profile becomes peaked. With a larger field, spiral arms with $m > 1$ are replaced by the $m = 1$ spoke mode, most clearly seen in plasma density. A transition from spiral arms to the spoke regime occurs when the plasma potential in the center changes from weakly positive (or zero) to negative. Further increase of the magnetic field results in a well-developed $m = 1$ spoke mode with additional small-scale higher frequency $m > 1$ structures inside and around the spoke. It is shown that while ionization and collisions affect some characteristics of the observed fluctuations, the basic features of the spoke and $m > 1$ spiral structure remained similar without ionization. The role of energy conservation in small-scale high-frequency modes and spoke dynamics is discussed. It is demonstrated that in regimes with the $m = 1$ spoke mode, additional $m = 4$ harmonics of the ion and electron fluxes to the wall appear due to the square boundary. The frequency of the $m = 1$ mode is weakly affected by the geometry of the boundary.

I. INTRODUCTION

Magnetic fields improve plasma confinement and are often employed to increase plasma density in low-temperature plasma devices. In typical applications with a moderate magnetic field, the electrons are fully magnetized and confined by the magnetic field while ions are only weakly affected by the magnetic field and can be controlled by the electric field. Instabilities that occur in such partially magnetized plasmas due to plasma inhomogeneities and electric fields have long been a subject of active studies, e.g. see Refs. 1 and 2 and references therein. Linear theory^{2,3} predicts a variety of instabilities that may occur in partially magnetized plasmas. However, nonlinear regimes and saturation of the instabilities have to be studied with numerical simulations.

A straight cylindrical configuration with an axial magnetic field and radial electric field (the so-called $\mathbf{E} \times \mathbf{B}$ configuration) is a prototype for the Penning discharges used in many technological applications⁴. One of the intriguing and important phenomena that dominate the radial plasma transport is a large-scale, $m = 1$ azimuthally rotating structure, the so-called spoke, typically observed as a large scale plasma density perturbation. Such spoke-type structures and multiple helicity modes in partially magnetized $\mathbf{E} \times \mathbf{B}$ plasmas were observed experimentally in Penning and other $\mathbf{E} \times \mathbf{B}$ plasma systems⁵⁻¹³ and also studied in numerical simulations under various conditions¹⁴⁻¹⁸.

Here, we study the spoke and spiral arms structures in a 2D radial-azimuthal geometry using Particle-in-Cell (PIC) WarpX code¹⁹. We study the square as well as the circular geometry of the external boundary. In both cases, Cartesian mesh is used thus avoiding the issues related to the region near $r = 0$ in the cylindrical coordinates. The code is run on the Mist server, <https://docs.scinet.utoronto.ca/index.php/Mist>, of the Digital Research Alliance of Canada with one GPU of NVIDIA V100-SMX2-32GB type per one separate simulation. The general setup of simulations is similar to that of Ref.20. Here we focus on the conditions for the spoke and spiral arms formations, the role of ionization, and consider the low pressure discharge of 0.44 mTorr while the higher pressure of 40 mTorr was considered in Ref. 20. In this paper, we propose the mechanism for the spiral arms formation, show the coexistence of the $m = 1$ spoke and $m > 1$ small-scale high-frequency modes, and demonstrate that geometrical effects of the square boundary result in the modulation of the electron and ion fluxes to the wall at the fourth harmonics of the spoke frequency.

To clarify the role of the ionization processes in the mechanism of the spoke, we have performed the simulations by turning off all collisional processes (including the ionization) and replacing the ionization with equivalent electron and ion sources. In this study, we observe the formation of the $m = 1$ spoke with roughly similar characteristics, thus demonstrating that the mechanism of the spoke instability is not related to the ionization processes.

In Section II, the PIC simulation model, and the parameters of simulations are described in detail. In Section III, we investigate the role of the electric field in the structure excitation and demonstrate the transitions between the $m > 1$ spiral arms and the $m = 1$ spoke regimes. The role of energy conservation in the spoke formation is discussed in Section IV. In Section V, we show the coexisting $m = 1$ spoke and multiple $m > 1$ high-frequency modes. The effect of ionization on the spoke formation is discussed in Section VI. In Section VII, we examine the effects of geometry on the spoke dynamics. Section VIII provides a summary and discussion of the results.

II. THE SIMULATION MODEL

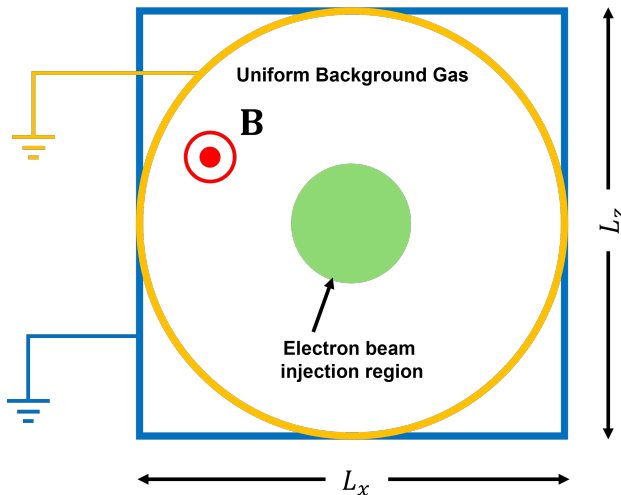


Figure 1: The cross-section of the modeling region. The base case simulations are performed with a square boundary. Section VII simulations are done with a circular boundary. The potential of the boundary is zero in all cases.

The setup of our numerical experiments aims to reproduce the conditions similar to experimental conditions for Penning discharges and ion plasma sources^{7,12,13,21}. In our simu-

lations, plasma discharge is supported by the ionization from the energetic electrons injected along the magnetic field in the y -direction (outward of the page in Fig. 1). The electron beam is uniform and injected into a circular region of a radius $R = 1.5$ cm, Fig. 1. In addition to one-step electron impact ionization $Ar + e \rightarrow Ar + e + e$, for electrons with the energy above 15.7 eV, excitation reactions $Ar + e \rightarrow Ar^* + e$, with the excitation energy of 11.55 eV, and elastic collisions are included. The electron-neutral isotropic scattering cross-sections included in WarpX distribution were sourced from Ref. 22, excitation cross-sections from Ref. 23, and ionization cross-sections from Ref. 24. The beam electrons are injected along the magnetic field in the direction opposite to the field with $E_b = 30$ eV axial energy and Maxwellian $T_e = 5$ eV temperature throughout the whole simulation duration. The background neutral gas is maintained at a constant density throughout the entire simulation. The injected electron beam is represented by macroparticles introduced at each simulation time step, corresponding to the total beam current of 1 mA. Technically, in two-dimensional geometry, which neglects the third direction, the injected current along the unresolved direction should be measured in units of the current per unit of length, A/m. This dimension however can also be absorbed directly into the cell volume²⁵, allowing the units of the injected current to remain in Amperes. The parameters of the simulations for the base case are given in Table I.

The 2D simulations are performed on a uniform Cartesian grid in the $x - z$ plane, with particle velocities in 3D $v_x - v_y - v_z$ space. A uniform axial magnetic field in the y direction is applied perpendicular to the simulation domain, all incoming particles are absorbed at the outer boundary with Dirichlet conditions for the potential, $\Phi = 0$. In the base case simulations, we use the rectangular geometry for the discharge boundary, as shown in Figure 1. In the Section VII, we examine the effect of a circular grounded boundary.

The simulations domain spans $L_x = L_z = 10$ cm and is discretized into a grid of $n_x \times n_z = 256 \times 256$ cells in the x - and z - directions, resulting in a mesh resolution of $\Delta x = 0.39$ mm. This resolution adequately resolves the Debye length through the simulations, as confirmed by direct calculations of electron temperature and plasma concentration in each cell. For the parameters of our simulations, at the center of the domain with, $B = 100$ G, we obtain the density of $n = 10^{15}$ m⁻³, and temperature of $T_e = 5.5$ eV. This results in a ratio of Debye length to mesh resolution of $\lambda_D/\Delta x = 1.41$. Similarly, the minimum ratio for a magnetic field of $B = 50$ G is 2, and for $B = 220$ G the Debye length is resolved by a factor of 4.

The simulation time step is $\Delta t = 50$ ps that resolves the electron cyclotron period and local plasma oscillation period satisfying the practical criteria of $\omega_{pe,ce}\Delta t < 0.2^{26}$. Electron cyclotron frequency for simulation with magnetic field of $B = 100$ G is $\omega_{ce} = 1.75 \times 10^9$ rad/s, and the characteristic value of plasma frequency is $\omega_{pe} = 1.78 \times 10^9$ rad/s for $n_p = 10^{15}$ m $^{-3}$. The spatial grid and time step are chosen to ensure that the Courant-Friedrichs-Lewy (CFL) condition is comfortably met. For the fastest particles, whose velocity is approximately equal to $v \approx 3v_{the} = 4 \times 10^6$ m/s for temperature $T_e = 5$ eV we have: $CFL = \sqrt{2}v\Delta t/\Delta x < 1$. The weight of a single macroparticle was equivalent to 312500 of real particles for simulations with Argon gas, both for electrons and ions. This value results in an average of 145 particles per cell (PPC). In simulations, the magnetic field is included for electrons and ions. Plasma remains quasineutral to a high degree on average and for perturbations, as seen from the comparison of electron and ion densities in Fig. 2.

In simulations, injected electrons' energy exceeds Argon atoms' ionization energy and most of the energy for ionization is provided by the electron beam. Additional energy can be deposited from the radial current and potential drop across the radial direction²⁰.

Table I: Physical parameters for the base case simulations with Argon.

Property	Symbol	Value
Magnetic Field	$B(\text{G})$	10, 50, 100, 220
Electron beam energy	$E_b(\text{eV})$	30
Electron beam current	$I_e(\text{A})$	0.001
Neutral temperature	$T_n(\text{K})$	300
Neutral pressure	$P_n(\text{mTorr})$	0.44
Neutral density	$n_n(\text{m}^{-3})$	1.4×10^{19}

Our study does not consider axial losses and ion collisions, thus all ions created by ionization reach the grounded electrode radially. In the actual 3D geometry, a fraction of ions created by ionization is lost axially. Since our simulations do not include the y-direction, such axial losses are not accounted for. Assuming that all ions are collected radially by the grounded electrode is a reasonable approximation for a discharge that is very long in the axial direction, since the axial losses scale as $R/L < 1$, where R and L are the characteristic dimensions in radial and axial directions, respectively. Although axial losses

could theoretically be simulated in 2D geometry by removing ions at a certain rate, this was not done in this study. At 0.44 mTorr, the ion mean free path is large and ions can be assumed collisionless. Investigating these effects and developing methods to represent boundary conditions along the y-axis in a 2D model are left for future work.

III. THE AZIMUTHAL STRUCTURES AND MODE TRANSITIONS

In this section, we demonstrate the sequence of transitions in the structure of the azimuthal modes occurring in the discharge as the magnetic field is increased. Figure 2 displays a sequence of 2D maps representing the electron and ion density for four values of the magnetic field from 10 G (the first row) to 220 G (the last row). Figure 3 shows the radial profiles of plasma parameters for the same values of the magnetic field. Note that while Fig. 2 shows instantaneous values, Fig. 3 shows time-averaged radial plasma parameters in the saturated state. The time window averaging for $B = 10$ G and $B = 50$ G is the last 500 μ s. For $B = 100$ G, it is the last 1960 μ s, equivalent to 6 spoke cycles. For $B = 220$ G, it is the last 2000 μ s, equivalent to 50 spoke cycles.

At the lowest magnetic field intensity of $B = 10$ G, one observes mostly uniform (symmetric) plasma density with little signs of any structures. For the larger magnetic field of $B = 50$ G, we observe the excitation of the azimuthal $m > 1$ spiral arm structures, Fig. 2b. Similar structures were also observed in simulations of Ref. 27. Further increase of the magnetic field to $B = 100$ G results in a large scale $m = 1$ coherently counterclockwise rotating structure along with $\mathbf{E} \times \mathbf{B}$ drift, the so-called spoke. The $m = 1$ slowly rotating structure coexists with fast spiral $m > 1$ modes that occur at the edges and inside of the $m = 1$ mode. Further increase of the magnetic field to $B = 220$ G leads to a more intense and violent spoke structure which also shows additional structures (blobs) that break away and move radially from the rotating spoke. One can note in Fig. 3a that with increasing magnetic field plasma confinement is improving resulting in higher plasma density. This trend persists from $B = 10$ G to $B = 100$ G. However, one observes that for $B = 220$ G, the average plasma density drops again due to the large radial transport from the intense spoke and radially moving density patches/blobs.

The transition from the quiescent state at $B = 10$ G to the spiral arms and then to the spoke at a higher magnetic field is a result of marked changes in the radial electric field.

For low magnetic field values ($B = 10$, and $B = 50$ G), the radial electric field is zero or mildly positive while for the stronger field the radial electric field changes sign and becomes negative (inward). Figures 2 and 4- 6 present the snapshots of the characteristic behavior of plasma parameters in the transition from spiral arm structure to spoke structure.

The spiral arms structures appear in the regime with zero or weakly positive electric field as it was also shown in our earlier simulations²⁰. It was suggested in Ref. 27 that the spiral arms structures are the result of the resistive (dissipative) gradient drift instabilities. Such instabilities are essentially driven by the current perpendicular to the magnetic field and can be induced either by the electron or ion flow (or both). They belong to the class of negative energy perturbations that can become unstable due to the dissipative²⁷⁻²⁹ or collisionless³⁰ mechanisms. Here, we suggest that the $m > 1$ spiral arms structures in the low B regime, Fig. 4b, occur as a result of the ion radial motion. In the low B case, in the stationary state, the ions move radially outward due to a weak radial (outward) ambipolar electric field formed by the electron losses to the external boundary. The ion radial motion results in the spiral arms' perturbations moving radially and azimuthally in the direction of the electron diamagnetic drift. Spiral arms arise due to perturbations of density, which come from the combined radial motion of ions and density/potential perturbations propagating azimuthal. The azimuthal motion of ions occurs due to the azimuthal perturbation of potential, respectively, due to the azimuthal electric field.

An increase in the axial magnetic field enhances electron confinement, forming a potential well and resulting in the inward electric field that triggers the collisionless Simon-Hoh mode for $\mathbf{E} \cdot \nabla n_0 > 0$ leading to the spoke excitation^{3,5,6}, also consistent with our results in Ref. 20. The flow of ions, which is strongly controlled by the electric field, remains coherent within the spoke structures as seen in Figs. 4 and 5. Unlike ions, strongly magnetized electrons are subject to $\mathbf{E} \times \mathbf{B}$ and diamagnetic drifts. Their motion is less coherent, Figs. 4 and 5. It is important to note that ions are weakly magnetized but still subject to the magnetic field's Lorentz force, which results in the deflection of their trajectories from the direction of the electric field. The measure of the magnetization is characterized by the parameter $E/rB\omega_{ci,ce}$ ^{31,32}. Magnetization is strong when this parameter is small, as for the electrons, when $B = 100$ G, $E = 0.5$ V/cm, $r = 3$ cm, $E/rB\omega_{ce} \simeq 10^{-4}$ they experience simple $\mathbf{E} \times \mathbf{B}$ and diamagnetic drifts. For argon ions, $E/rB\omega_{ce} \simeq 7$ and ion motion is strongly affected by the inertia (centrifugal forces) and deviates from the $\mathbf{E} \times \mathbf{B}$ velocity²⁰. For larger values

of the magnetic field, ion magnetization may increase, however, the electric field, which is controlled by plasma transport, is also increasing. As a result, in our simulations, for a larger magnetic field of $B = 220$ G, ions remain weakly magnetized. Effects of finite ion magnetization on the Simon-Hoh instability were considered in Refs. 31 and 32.

The electron and ion temperature in Fig. 6 follow the behavior of the observed structures. The improvement of electron confinement with the magnetic field results in a higher density of energetic electrons in the central part of the discharge, Figs. 6b and 6d. The ions are collisionless here and their effective temperature corresponds to the energy of trapped ions bouncing in the potential well. The ion Larmor radius corresponding to the well depth is about 0.02 m or larger, which is in the order of the system radius of 0.05 m. Also, the potential well is not stationary: it is deformed and is rotating with the spoke motion so the ions escape radially as a result of the azimuthal (spoke) rotation driven by the azimuthal electric field. The electron Larmor radius remains smaller than the system size, providing effective magnetic confinement for electrons throughout the domain.

IV. ROLE OF ENERGY CONSERVATION IN THE SPOKE FORMATION

Most of the simulations reported in this paper have been performed with the energy-conserving algorithm using the so-called Yee grid available in WarpX. For the electrostatic case, the main feature of the Yee grid is that the electric field is stored in the cell centers, contrary to the collocated grid where the electric field is defined on the nodes. The latter option, resulting in the momentum-conserving scheme is also available in WarpX. We have performed spoke simulations with both options, the collocated grid (momentum-conserving) and the Yee grid (energy-conserving). In the simulations with the momentum-conserving scheme, we observe unnatural checkered patterns at small scales and higher frequencies, and the shape of the $m = 1$ large scale structures is also distorted as shown in Fig. 7 (left). It was found that these simulations have had energy errors of the order of 30 – 50%. Similar checkered patterns, spoke distortions, and energy errors were also observed in our situations with EDIPIC-2D which uses the momentum-conserving scheme (these results are not reported here). The simulations with an energy-conserving Yee grid demonstrate a much clearer picture of $m = 1$ structure and small-scale fluctuations inside. It is interesting to note that the energy errors appeared in the case when the $m = 1$ spoke and small-scale

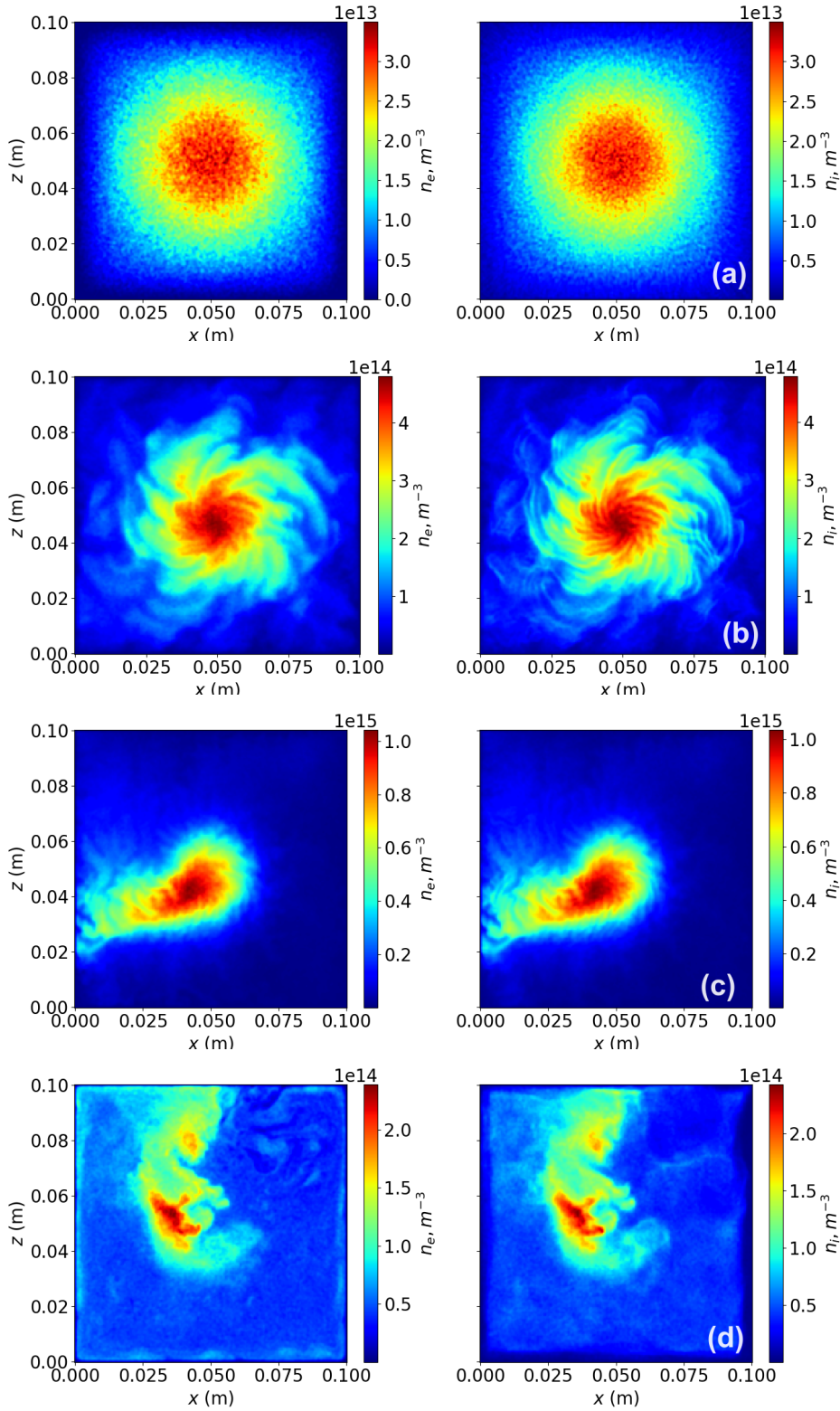


Figure 2: Snapshots of the electron (left) and ion (right) densities for the different magnitudes of the magnetic field: (a) $B = 10$ G at 6.71×10^{-4} s; (b) $B = 50$ G at 8.86×10^{-4} s (YouTube video); (c) $B = 100$ G at 2.96×10^{-3} s (YouTube video); (d) $B = 220$ G at 1.27×10^{-3} s (YouTube video).

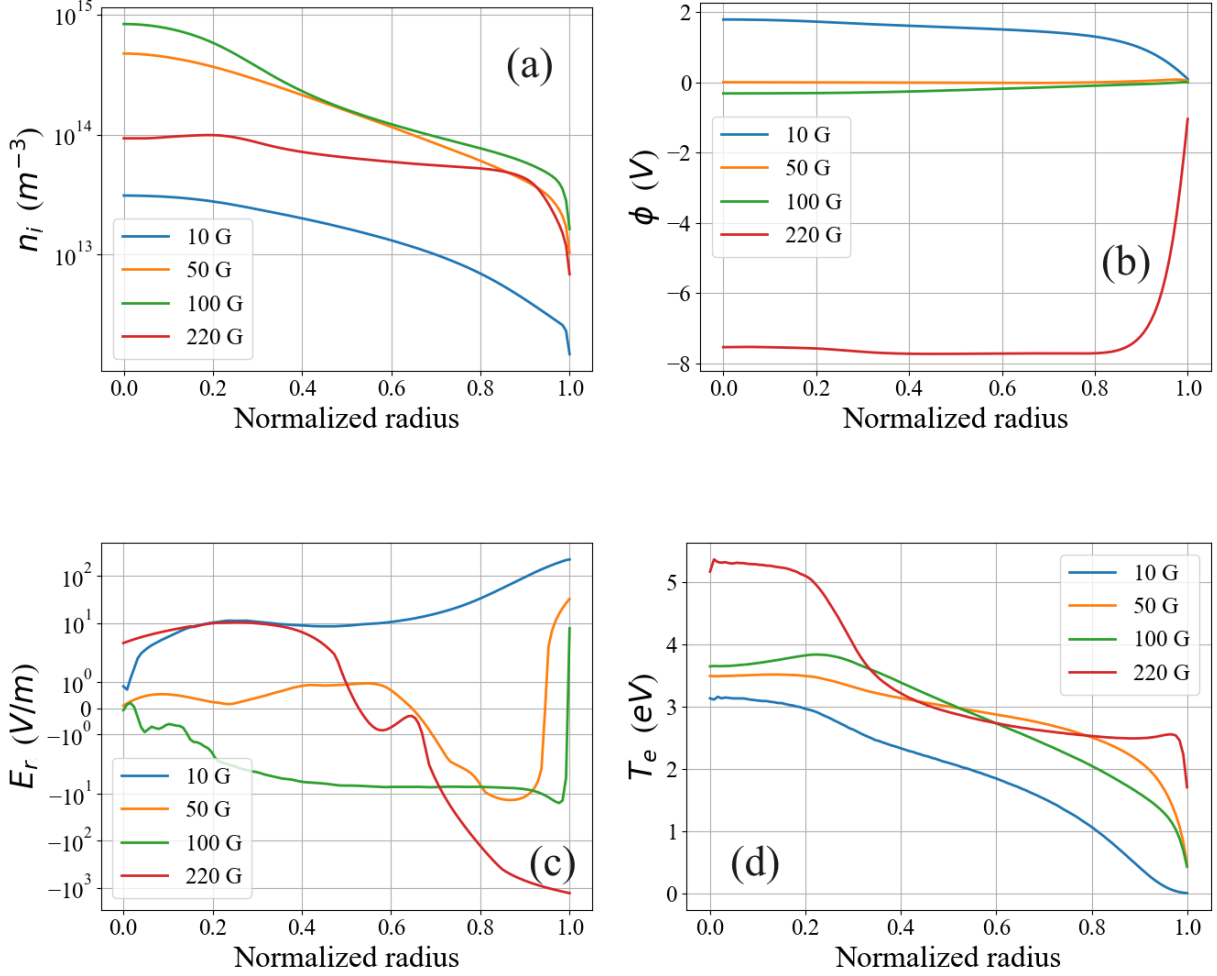


Figure 3: Averaged radial profiles of plasma parameters for different magnitudes of the magnetic field, the radius from the center of the domain is normalized to the largest radius which is 5 cm, so the normalized injected radius is located at 0.3: (a) ion density; (b) potential; (c) electric field; (d) electron temperature.

fluctuations coexist. We have not observed energy conservation problems in our earlier EDIPIC simulations²⁰ of the spoke in high neutral pressure regimes which did not have appreciable levels of coexisting small-scale structures. Similar spoke behavior and energy errors in simulations with the momentum-conserving schemes were found in simulations with two independent PIC codes performed at LAPLACE laboratory³³. It was also found in these simulations³³ that higher resolution in momentum-conserving schemes improves energy conservation but does not completely solve the problem. Accuracy and advantages of the energy-conserving PIC algorithms were discussed in recent works^{34,35}.

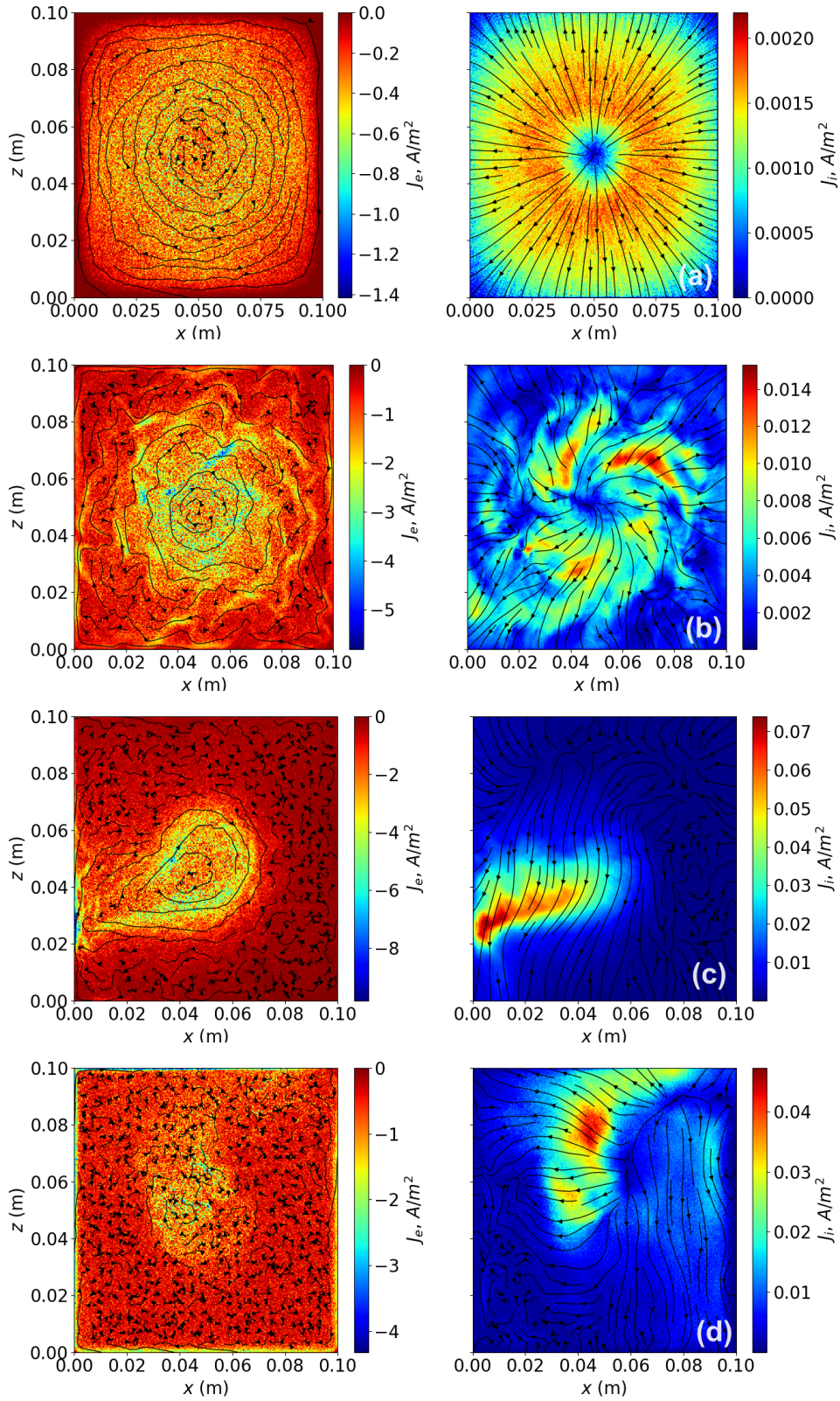


Figure 4: Snapshots of the electron and ion current density, with arrows for the direction and colors for the current magnitude: (a) $B = 10$ G; (b) $B = 50$ G; (c) $B = 100$ G; (d) $B = 220$ G; shown at the same time moments as in Fig.2.

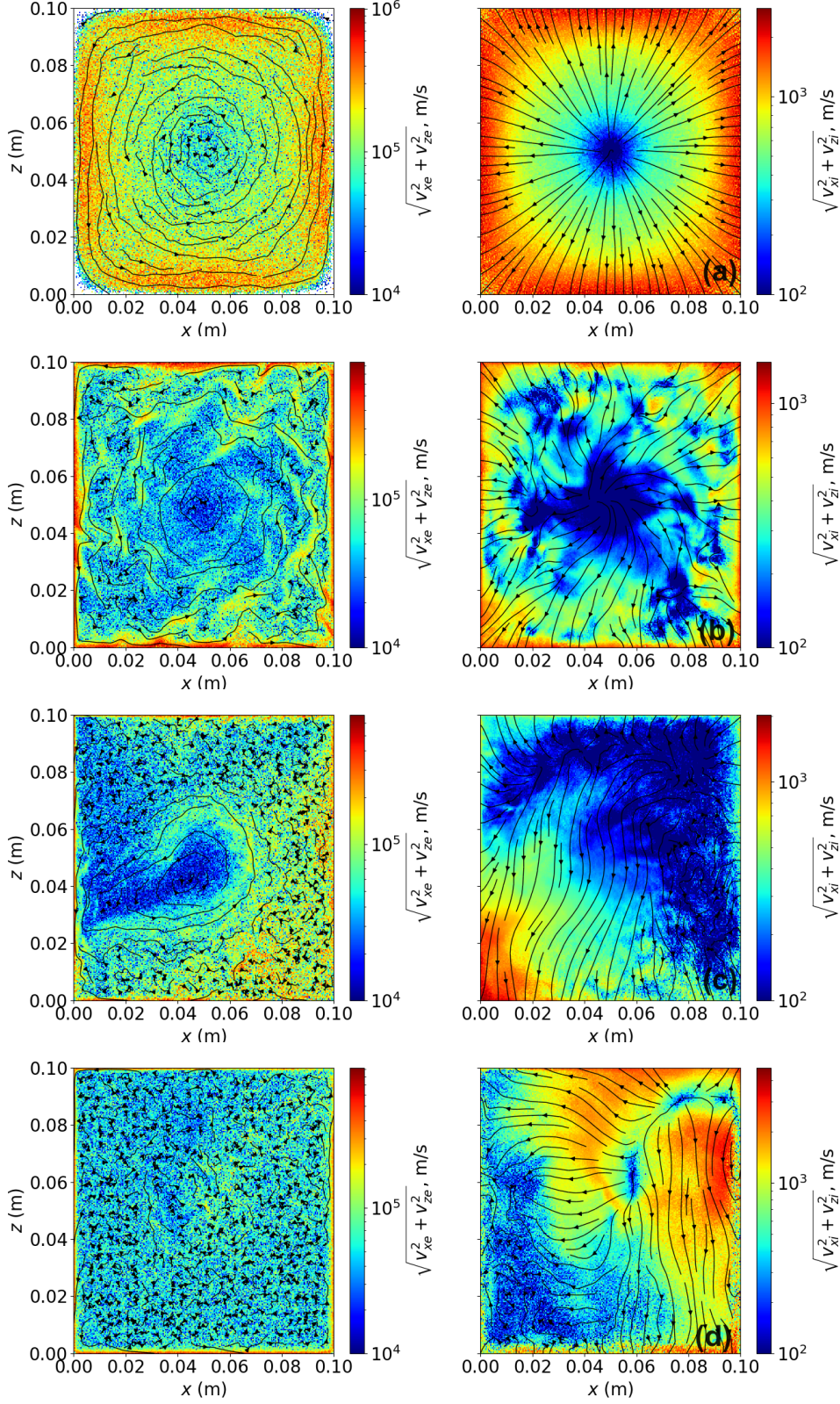


Figure 5: Snapshots of the absolute value of the electron and ion velocity with the direction vectors for the different magnitude of the magnetic field: (a) $B = 10$ G; (b) $B = 50$ G; (c) $B = 100$ G; (d) $B = 220$ G; shown at the same time moments as in Fig.2.

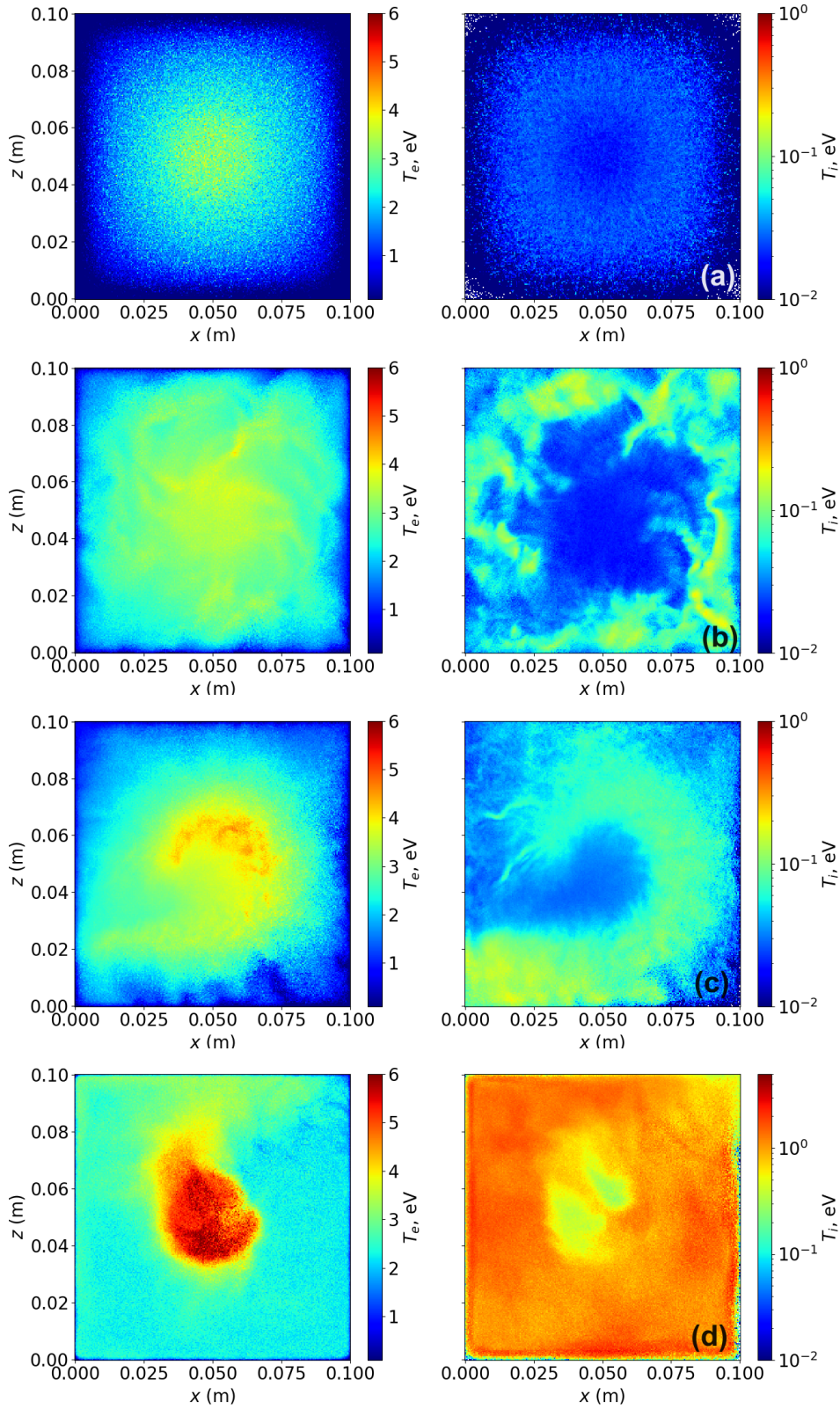


Figure 6: Snapshots of the electron (left) and ion (ion) temperatures for the different magnitude of the magnetic field: (a) $B = 10$ G; (b) $B = 50$ G; (c) $B = 100$ G; (d) $B = 220$ G; shown at the same time moments as in Fig.2.

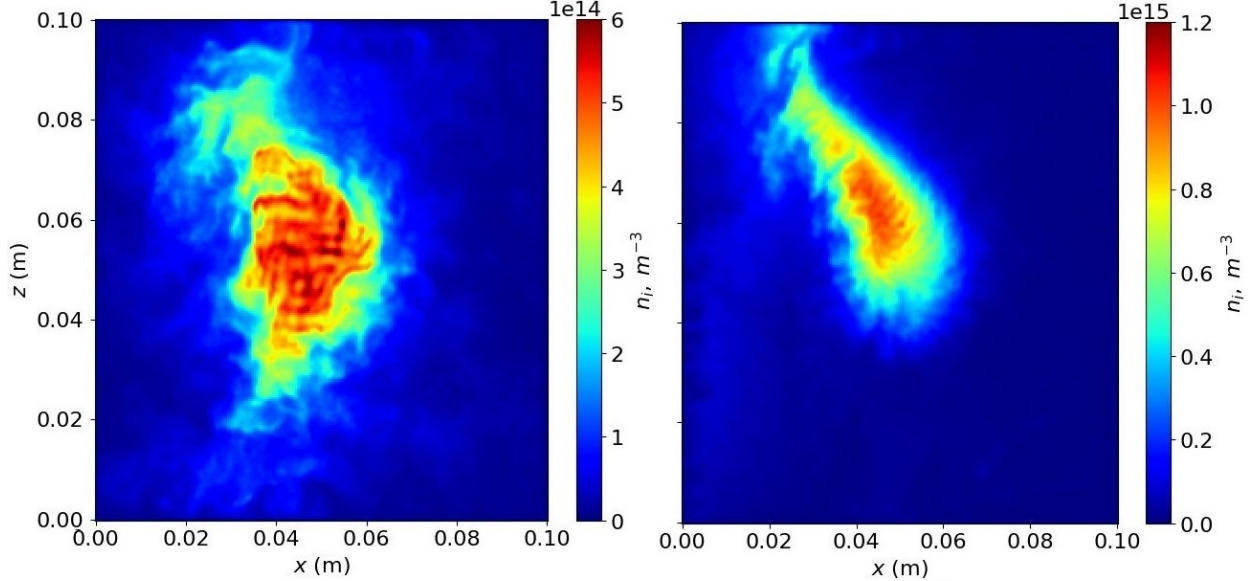


Figure 7: The ion density perturbations in simulations using the collocated grid (left) at 5.68×10^{-3} s and Yee grid (right) at 4.9×10^{-3} s for $B = 150$ G and 1 mA current

V. COEXISTING SPOKE AND HIGH-FREQUENCY SMALL-SCALE STRUCTURES.

As it has been already noted above, the large scale $m = 1$ spoke is accompanied by higher frequency small scale structures as is apparent in density snapshots in Fig. 2c. The coexistence of spoke and high-frequency small-scale structures becomes even more pronounced in simulations with a larger value of the injected current of 100 mA (high current case) as shown in Fig. 8. For this case, the simulation time and spatial steps were decreased to $dt = 10^{-11}$, and the mesh size is 1024×1024 to maintain the same CFL number. The weight of a single macroparticle for both species is 6250000 particles. The magnetic field strength is 150 G. The small-scale fluctuations have a spiral arm structure and higher frequency. The MUSIC (multiple signal classification)³⁶ spectra analysis shows the frequencies of the density spiral arms structures in the range of 10^2 kHz, Fig. 9. They are more pronounced in the region closer to the center of the discharge, at a distance of $L/16$ from the center. The density probe at a larger distance, $L/4$, shows intense harmonics of the main spoke frequency in the range of 10 kHz and lesser amplitude of the 10^2 kHz high-frequency modes. The general behavior of the electron and ion current and temperatures is shown in Figs. 10 and 11, is similar to the base case with the current of 1 mA (low current case). One should

note an elevated ion temperature in Fig. 11 on the outside of the spoke structure. We believe this is a result of the ion heating from the small-scale high-frequency lower-hybrid fluctuations which are destabilized by the density gradients across the spoke boundaries. The presence of fluctuations in the range of the lower-hybrid frequency is confirmed by Fast Fourier Transform spectra of the radial and azimuthal electric field obtained from the probe data as shown in Fig. 12.

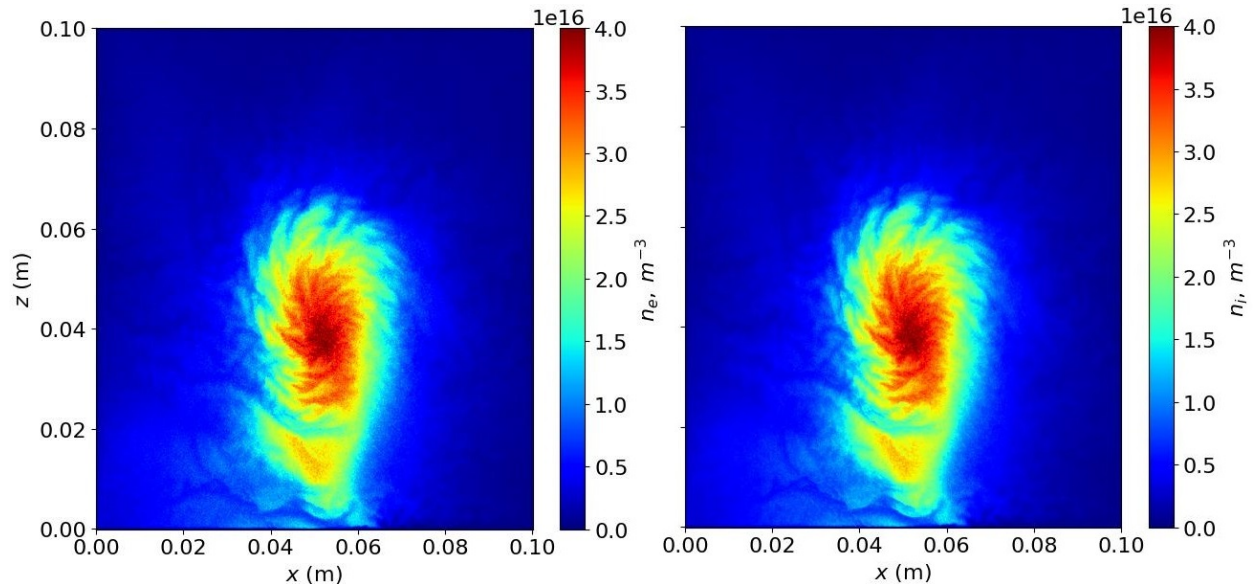


Figure 8: High-frequency small-scale structures inside and on the periphery of the $m = 1$ spoke in the high current simulations 100 mA, $B = 150$ G; electron (left) and ion (right) density.

VI. SPOKE STRUCTURE IN SIMULATIONS WITH EXTERNAL PLASMA SOURCES AND THE ABSENCE OF E-N COLLISIONS

In many cases, the ionization processes are essential in the self-organization of plasma discharges resulting in the formation of nonlinear structures. This may occur either directly through the nonlinear dependencies of the ionization on electron temperatures (as in the formation of strata and striations³⁷) or via additional turbulence caused by instabilities resulting from the interactions between plasma and neutral flows. The latter mechanism is responsible for the phenomena of Critical Ionization Velocity (CIV), invoked for the spoke formation in some conditions³⁸.

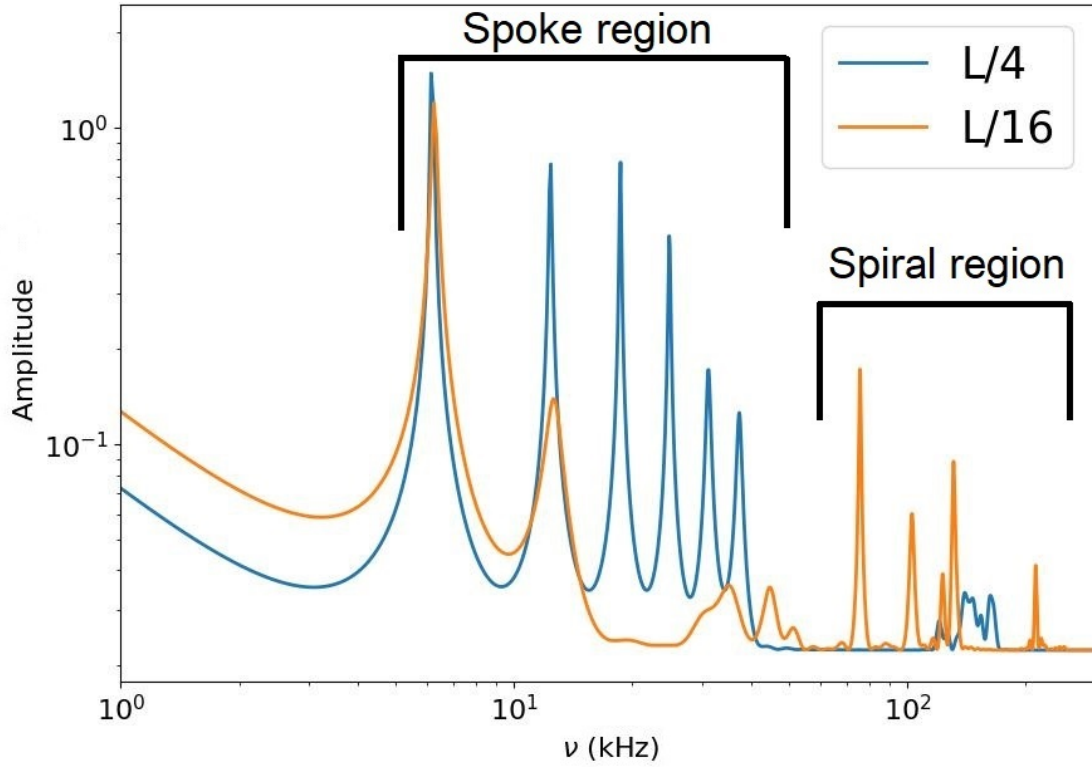


Figure 9: MUSIC spectra for probes at $L/4$ and $L/16$ distance from the center for simulations shown in Fig. 8.

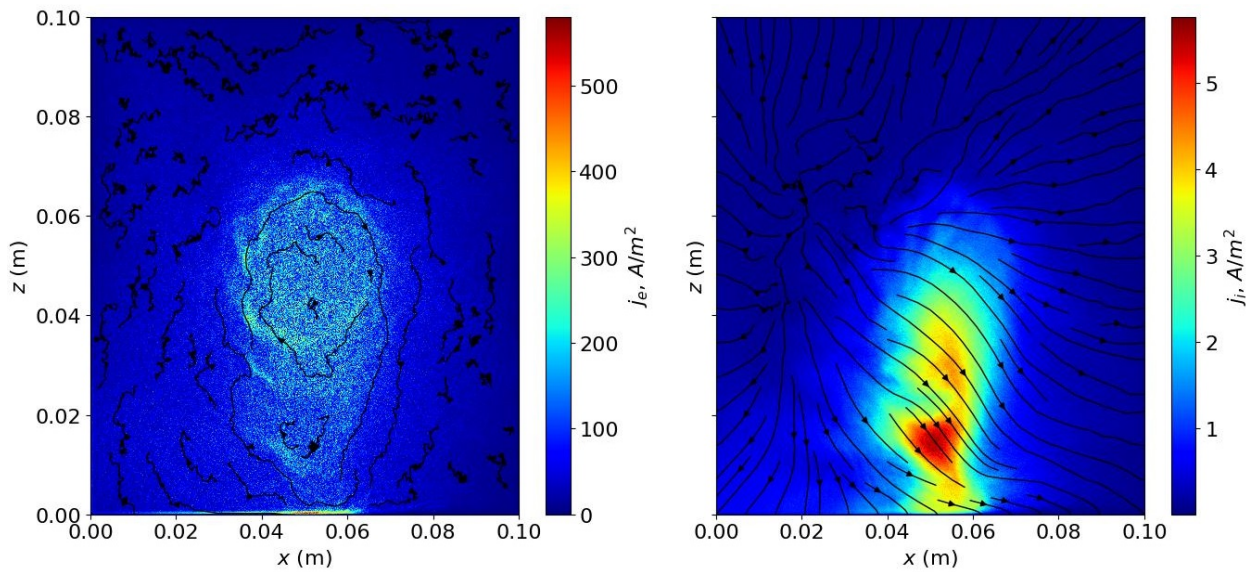


Figure 10: Electron and ion current densities in the high current spoke simulations
100 mA, $B = 150$ G.

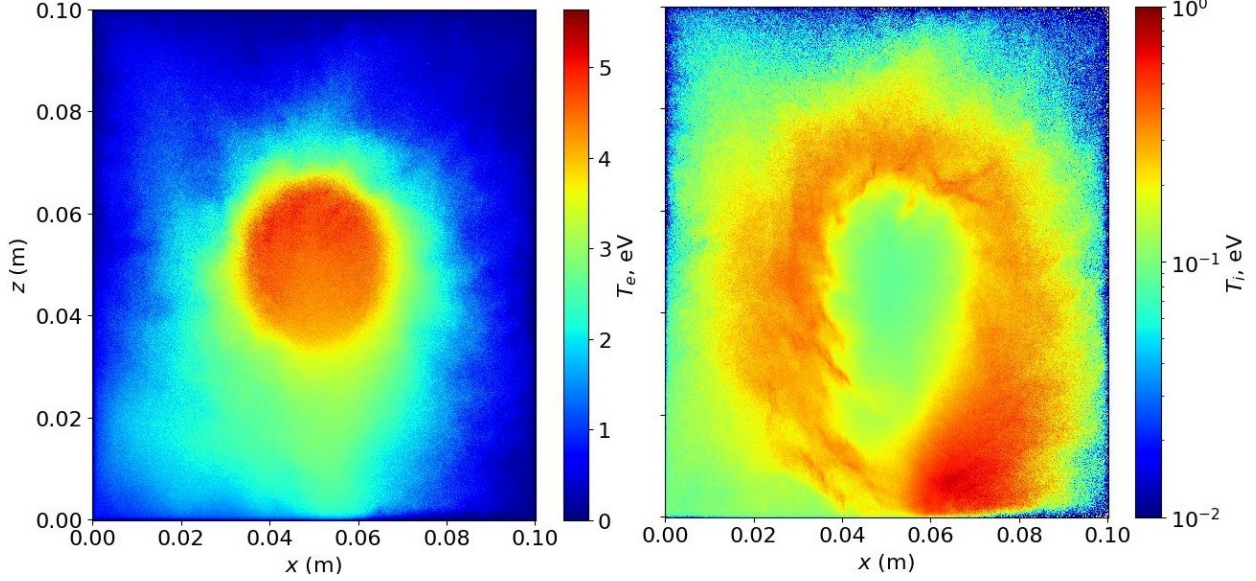


Figure 11: Electron and ion temperatures in the high current spoke simulations
 100 mA , $B = 150 \text{ G}$.

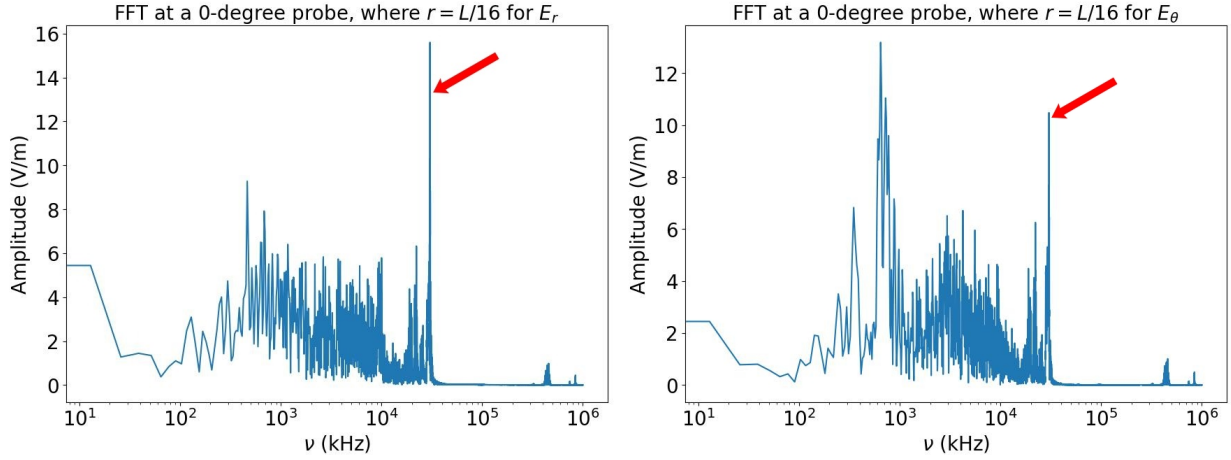


Figure 12: Fourier spectra for E_r and E_θ components of the electric field obtained from the probe data located at $\theta = 0$, $r = L/16$ from the center; the simulations with $B = 150 \text{ G}$ and 1 mA . The frequency at $3 \times 10^4 \text{ kHz}$ (shown by the red arrow) is consistent with the frequency of a lower-hybrid mode.

We have tested earlier a possibility of spoke formation due to CIV in our earlier spoke simulations in high-pressure regimes²⁰ where it was found that the spoke velocity is well below the CIV values. It is further suggested here that the ionization does not directly cause the mechanism of the spoke excitation. This has been confirmed here by the simulations in the absence of ionization where plasma discharge is supported by external sources of

electrons and ions.

For these simulations, we considered the regime with 1 mA and 150 G which has reached a steady state. At this stage, the electron and ion currents to the walls were $I_e = 2$ mA and $I_i = 1$ mA, respectively. The electron and ion temperature established in the injection region were $T_e = 5$ eV and $T_i = 0.1$ eV. Then, all electron-neutral collisions were turned off, and electrons and ions were generated in the circular region (as in Fig.1) at the rates corresponding to their currents and with the temperatures equal to their stationary values as above.

Figures 13-16 show the comparison of plasma parameters in the simulations with the ionization and with external sources in the absence of ionization. In general, one observes fairly similar behavior and structure patterns.

VII. EFFECTS OF THE GEOMETRY: OSCILLATIONS IN THE ION AND ELECTRON FLUXES

In our base case simulations with e-n collisions, we used a square box geometry of the external boundary. Various applications of the discharges with axial magnetic fields may use both circular and rectangular shapes as well as their combinations for the external boundaries^{4,12,13,39-41}. Therefore, it is of interest to explore the differences arising from the shape of the external boundaries. To change geometry to a circle we use what's called an embedded boundary object in WarpX. It allows the addition of curved boundaries to the system with rectangular geometry. In our case, we add a circle to our square geometry as an implicit function $(x - L_x/2)^2 + (z - L_x/2)^2 = (L_x/2)^2$ (see Fig. 1). This boundary has the same features as the rectangular boundary, absorbing all incoming particles and zero potential as a boundary condition for the solution of the Poisson equation. Figure 17 shows the evolution of the inventory of particles in the Argon discharge simulation within a circular boundary, as in Fig. 1, and compares it with the case of the square boundary. One observes a small difference in the total number of particles at the saturation, which can be explained by the difference in the plasma volume for the two geometries. The rotation frequencies of the spoke in square and circular geometries obtained from the Fourier Transform of the density perturbation in the $\theta - t$ are nearly identical as shown in Fig. 17b. The general shape of the density structures in the $m = 1$ spoke in the square and circular geometries are

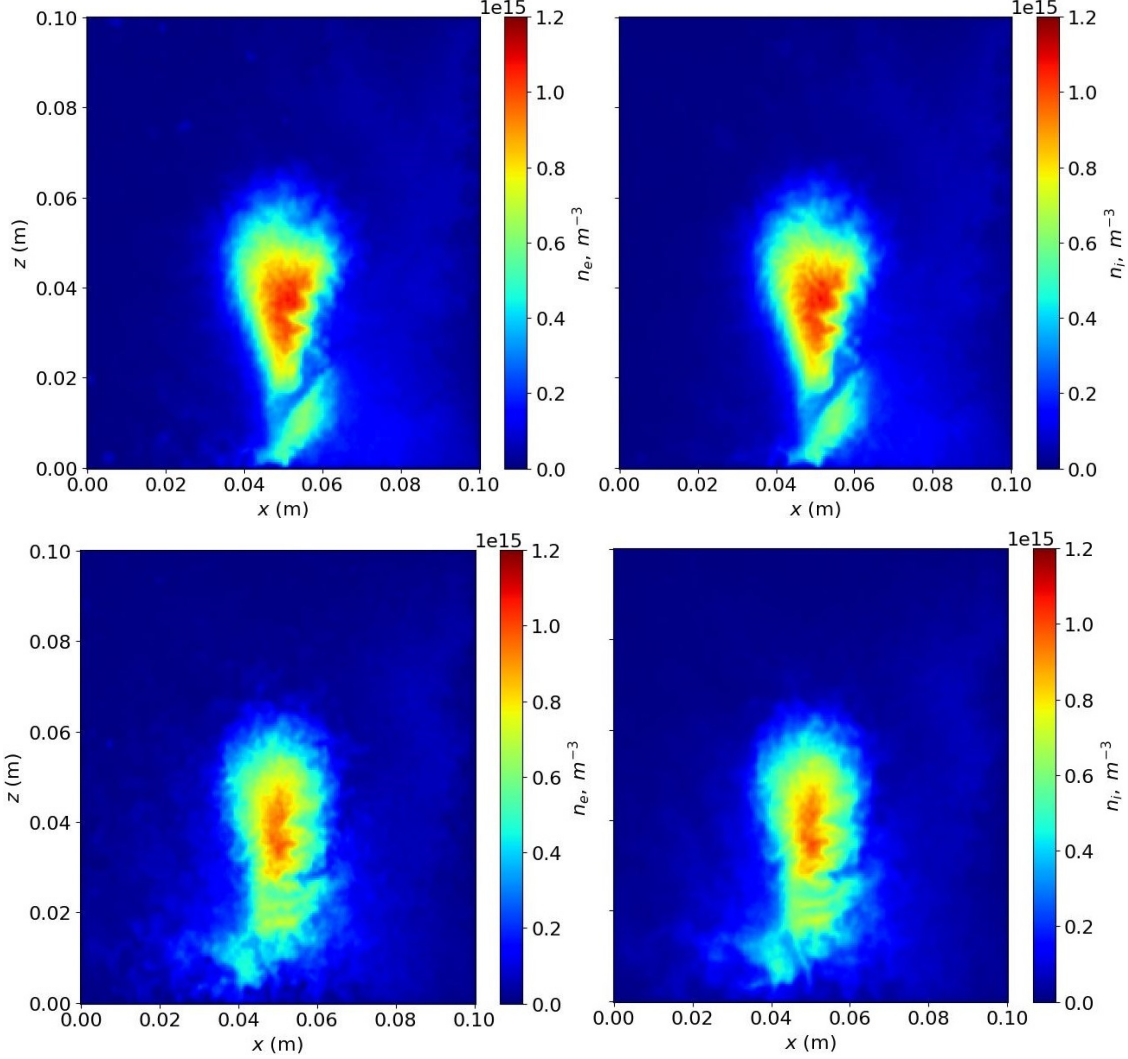


Figure 13: Electron and ion concentrations for the regime with ionization (top row) at 5.05×10^{-3} s, and with external sources (bottom row), at 6.46×10^{-3} s for $B = 150$ G and 1 mA current.

also very similar as shown in Figs. 18.

Despite these similarities, the geometry of the boundary introduces an essential difference in the electron and ion flows to the wall. Most easily, this difference can be seen in the temporal behavior of the total electrons and ion currents measured at the walls. Figures 19 show that the square boundary modulates the total electron and ion currents at the walls at a frequency roughly four times the spoke frequency. Note that the sum of the electron and ion current does not show these oscillations and is equal to the total injected current of 1 mA. It is worth noting that in both cases, with 1 mA and 100 mA electron beam injection, the value of the ion current due to the ionization is roughly equal to the electron

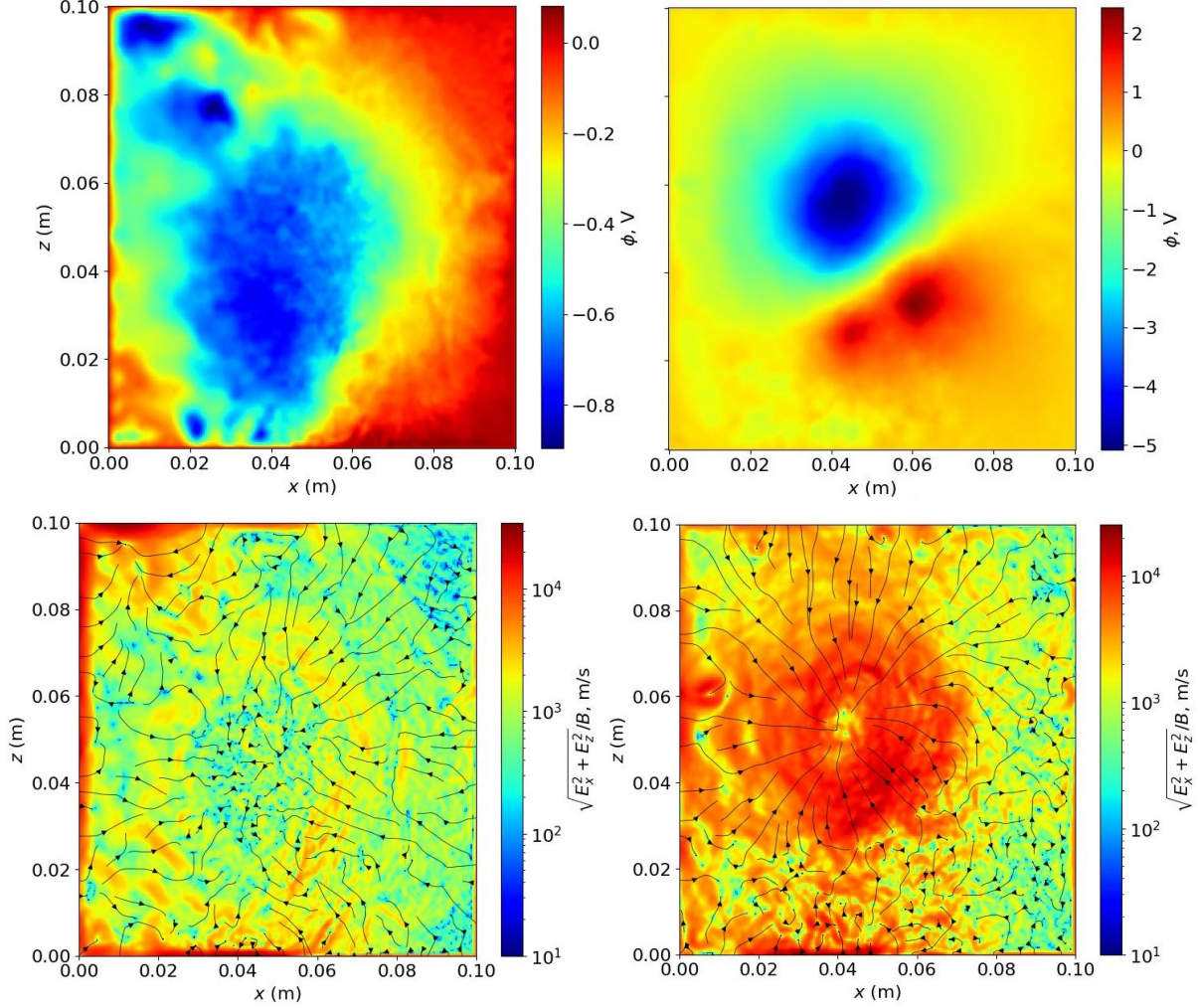


Figure 14: Top row: Potential map for the regime with the ionization (left) and with external sources (right). Bottom row: $\mathbf{E} \times \mathbf{B}$ velocity for the regime with the ionization and with external sources for $B = 150$ G and 1 mA current.

current induced by the ionization. Consequently, the electron current to the wall is roughly double the injected current.

The oscillations at the fourth harmonic of the spoke frequency are not related to ionization: Figs. 19 (a) and (b) exhibit similar oscillatory behavior, despite (a) being fully collisional and (b) collisionless and without ionization. Fig. 19 (c) shows that these geometry-induced oscillations disappear in the circular geometry. It is a result of geometrical modulations of particle losses as the spoke rotates against the square boundary. The modulations are also evident in the total particle inventories, as seen in Fig. 17.

The Fig. 19 (e) shows the square boundary-induced electron and ion oscillations for the

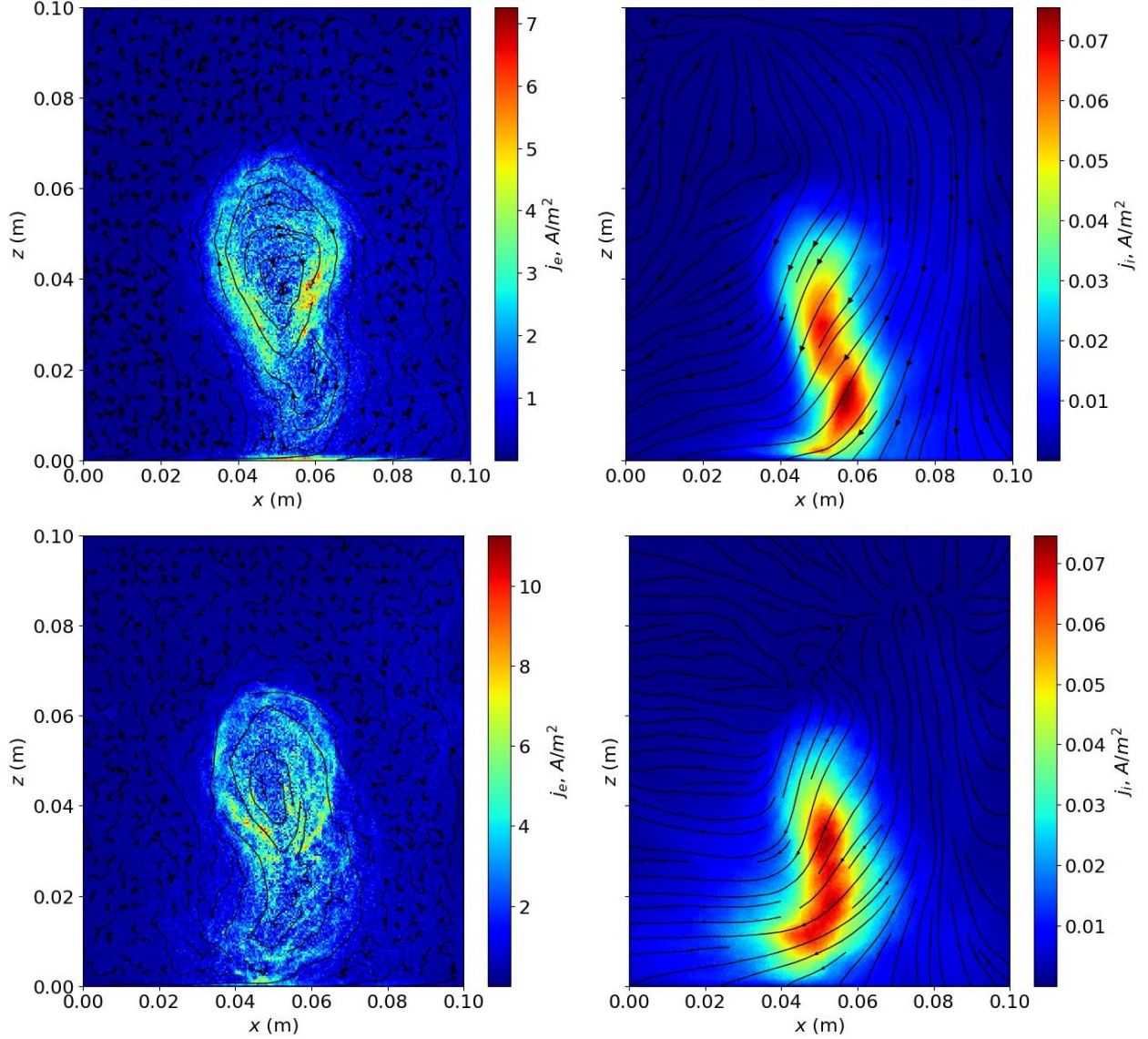


Figure 15: Electron and ion currents in the simulations with the ionization (top row) and with external sources (bottom row) for $B = 150$ G and 1 mA current.

case of 100 mA injections. In Fig. 20, we present the current density behavior for the 100 mA case at two different time frames: one at the moment when the spoke is perpendicular to the wall and the other – directed to the corner. The spoke-induced ion flow to the wall has both azimuthal and radial structure – note the radial propagating ion flow blobs propagating along the spoke. One can also note that the direction of the ion current is consistently deflected from the radial spoke direction as a result of the ion inertial forces.

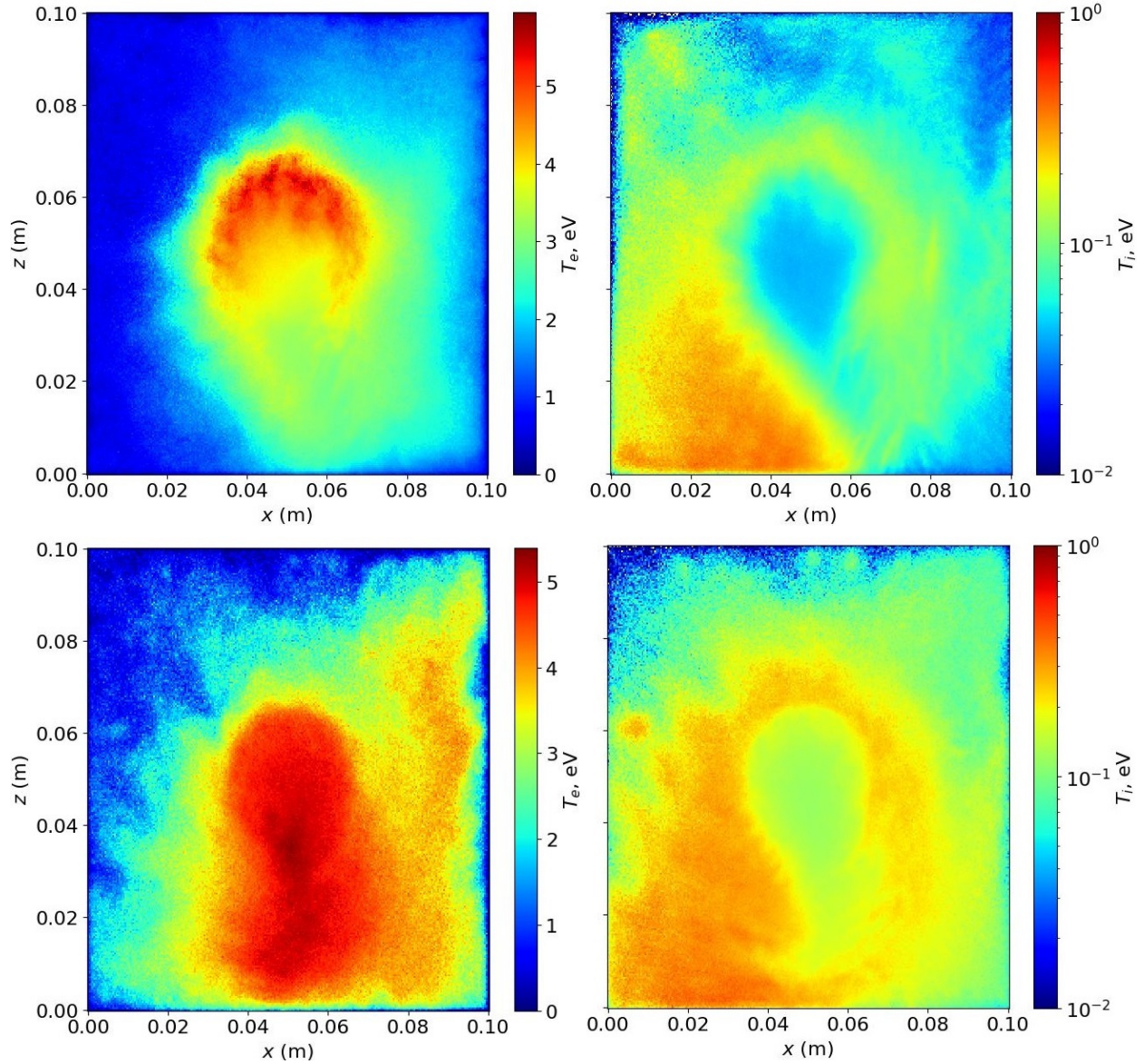


Figure 16: Electron and ion temperatures in the simulations with the ionization (top row) and with external sources (bottom row) for $B = 150$ G and 1 mA current.

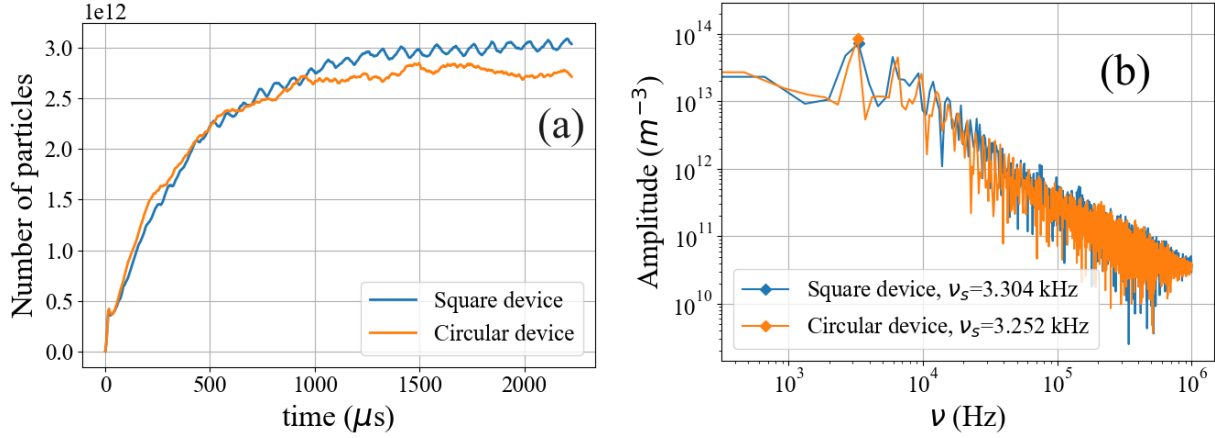


Figure 17: (a) Temporal evolution of the total number of particles (electrons + ions), and (b) spoke frequency of Argon gas in circular and square simulation geometry for $B = 100$ G and 1 mA current.

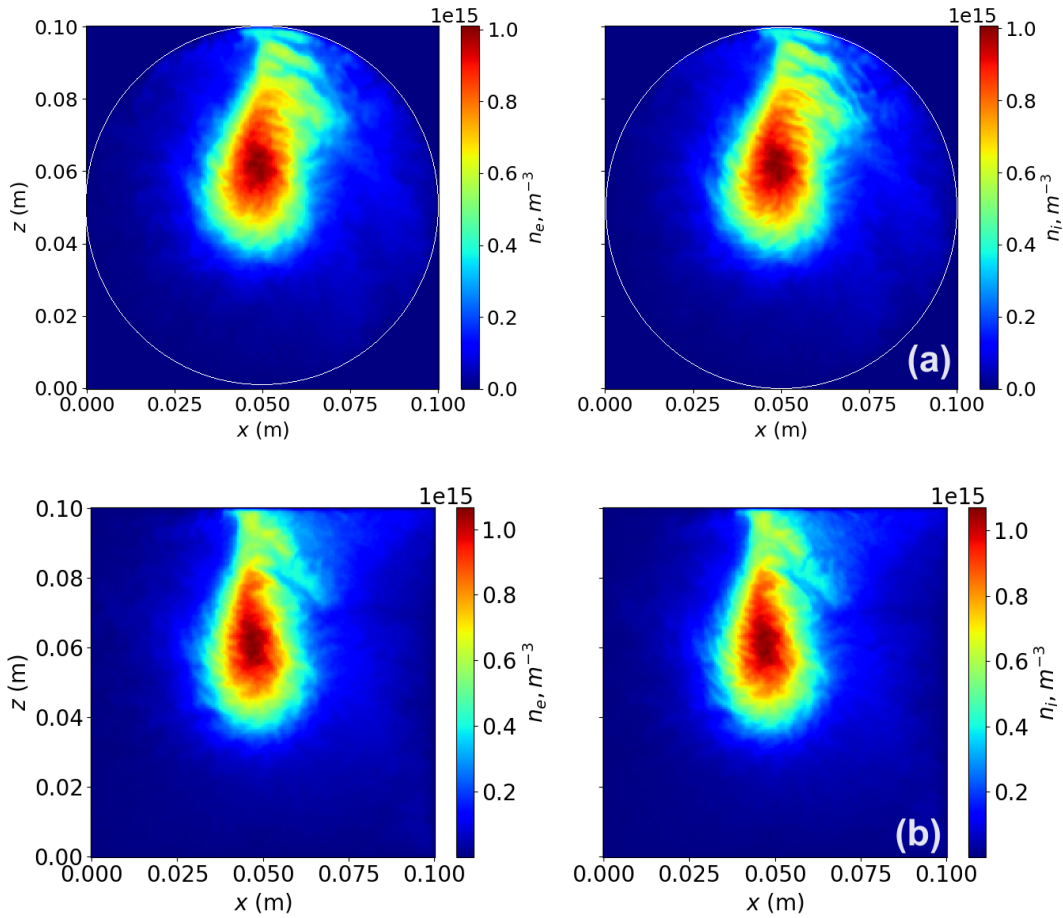


Figure 18: The electron and ion densities for the $m = 1$ spoke in (a) circular, white line shows the location of the circular boundary and (b) square boundary geometry for $B = 100$ G and 1 mA injection current.

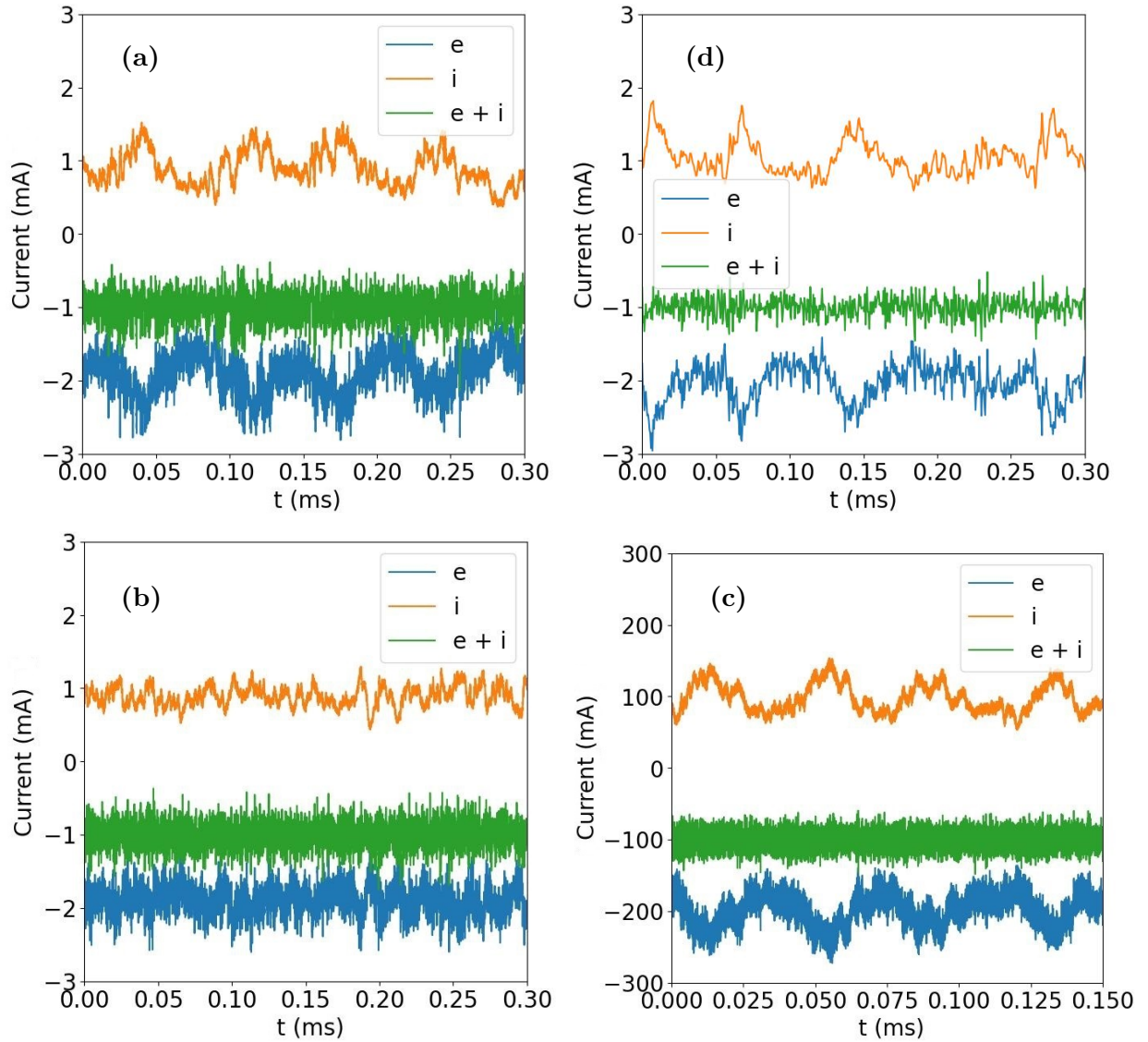


Figure 19: The total electron and ion currents at the boundary as a function of time for the square geometry and circular geometries: (a) square geometry with collisions and ionization, (b) square geometry with external plasma sources (in absence of collisions and ionization); (c) circular geometry with collisions and ionization, 1 mA injection; (d) square geometry with collisions and ionization, 100 mA injection. Note the absence of the oscillations for circular geometry, in all cases $B = 150$ G.

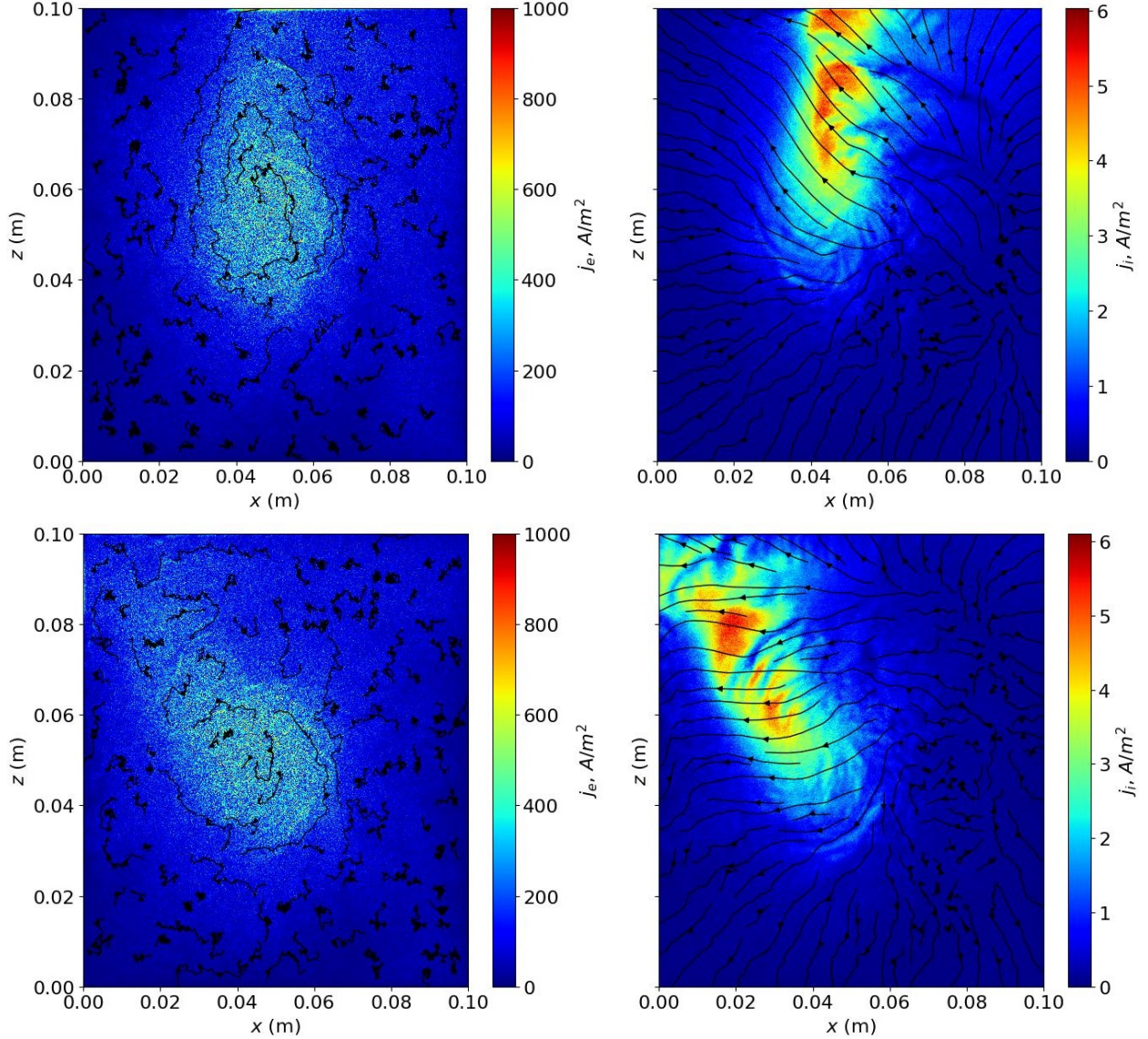


Figure 20: Electron and ion current densities for two time frames of a spoke in the 100 mA regime.

VIII. SUMMARY

In this paper, we have investigated the transitions between different types of azimuthal structures excited in $\mathbf{E} \times \mathbf{B}$ plasma self-consistently supported by the ionization from an axial electron beam. We show that multiple m spiral arm structures are excited in plasmas with zero (or slightly positive) radial electric field. With the increase of the magnetic field, electron confinement improves and a negative (inward) electric field is generated. At this point, the $m = 1$ spoke mode is excited in the discharge.

We suggest here that the excitations of the spiral arms are due to the instability caused by the combination of the density gradient and ion radial flow when the condition $\mathbf{v}_{i0} \cdot \nabla n < 0$ is satisfied as discussed in Ref. 3. Such instability generates modes with simultaneous propagation in the radial and azimuthal directions as is observed for spiral arms. As in Ref. 20, the excitation of the $m = 1$ spoke is explained as a result of the collisionless Simon-Hoh instability due to the radial electric field. This mechanism is related to the combined effect of the density gradient and the electron $\mathbf{E} \times \mathbf{B}$ drift due to the equilibrium radial electric field when $\mathbf{E} \cdot \nabla n > 0$. One has to note that the observed $m = 1$ spoke is not the most unstable linear mode. The linear theory predicts that the growth rate increases with $m^{2,3,5,32}$. For the higher m modes the effects of the electron inertia become important and the basic instability mechanisms due to the density gradient, the equilibrium electron and ion flows are modified, and the mode frequency shifts toward the lower-hybrid range. The dissipation due to the electron collisions may also provide additional destabilization^{3,27}. Direct excitations and interactions of small and large-scale modes were studied experimentally¹¹ and in simulations^{16,42}. Thus the $m = 1$ spoke mode should be viewed as a strongly nonlinear perturbation formed by the nonlinear interactions (inverse cascade) from the linear unstable high m modes.

In our simulations, we directly observe high-frequency small-scale modes coexisting with the $m = 1$ spoke. The high-frequency modes are observed in MUSIC and FFT spectra in density and electric field fluctuations. Another result observed in our simulations is the heating of cold ions generated by the ionization. Such heating, as is shown in Fig. 16, which increases the ion temperature to the range of ≈ 1 eV, is interpreted as a result of the lower-hybrid type modes. The ion heating is more pronounced in the simulations with external sources and the absence of ionization, comparing the ion temperature in the top and bottom rows (right column) of Fig. 16. Such ion heating has been observed in $\mathbf{E} \times \mathbf{B}$ plasma experiments²¹. The reduced heating in the simulations with ionization can be explained as a result of the collisional dissipation. We recall that in the simulations without ionization, the energy of the injected ions is $T_i = 0.1$ while the ion energy observed in the region outside of the spoke reaches $T_i \approx 1$ eV.

Our simulations without ionization further confirm the conclusions made in Ref.15 that the ionization is not essential for the spoke excitation. We have performed simulations replacing the ionization with external sources that produce electrons and ions at the same

rates and energies as in the self-consistent simulations with ionization. The observed patterns of the spoke and high-frequency small-scale modes remain similar suggesting that in these conditions gradient-drift instabilities, such as Simon-Hoh, are the primary sources of the observed structures. We have to note, however, that in some conditions the situation could be more complex. The spoke structures observed in direct current magnetron sputtering discharges are directly identified as moving ionization zones with enhanced emissivity where the ionization seems to be important^{43,44}. The difference with the modes considered here potentially may be related to the presence (in the magnetrons) of a strong electric field applied externally, as well as to the effects of the inhomogeneous magnetic field⁴⁵, where the ionization due to the electron heating provides an additional drive for the instability.

We demonstrate here the effect of the geometry of the external boundary on the electron and ion fluxes. It is shown that the square boundary modulates the electron and ion fluxes, at the frequency four times that of the spoke rotation. However, these modulations are not related to the modulation of the ionization so the total plasma source due to ionization is not modulated. It is worth noting that the probe measurements may detect modulation of the ion and electron fluxes by non-symmetric boundaries, which may be misinterpreted as a different (from the spoke) mode. Note that for the general non-circular geometry of the boundary, the frequency of the modulated electron and ion fluxes is not necessarily an integer multiple of the spoke frequency as in our case of the square boundary.

ACKNOWLEDGMENTS

This work is supported in part by NSERC Canada, SciNet-SOSCIP and the Digital Research Alliance of Canada, <https://alliancecan.ca/en>, and the Plasma Collaborative Research Facility at Princeton Plasma Physics Laboratory. This research used the open-source particle-in-cell code WarpX <https://github.com/ECP-WarpX/WarpX>, primarily funded by the US DOE Exascale Computing Project. Primary WarpX contributors are with LBNL, LLNL, CEA-LIDYL, SLAC, DESY, CERN, and TAE Technologies. We acknowledge all WarpX contributors. WarpX was run on the Mist server of SciNet-SOSCIP, <https://docs.scinet.utoronto.ca/index.php/Mist>.

DATA AVAILABILITY

The data that support the findings of this study are available from the corresponding author upon reasonable request.

REFERENCES

- ¹Igor D. Kaganovich, Andrei Smolyakov, Yevgeny Raitses, Eduardo Ahedo, Ioannis G. Mikellides, Benjamin Jorns, Francesco Taccogna, Renaud Gueroult, Sedina Tsikata, Anne Bourdon, Jean-Pierre Boeuf, Michael Keidar, Andrew Tasman Powis, Mario Merino, Mark Cappelli, Kentaro Hara, Johan A. Carlsson, Nathaniel J. Fisch, Pascal Chabert, Irina Schweigert, Trevor Lafleur, Konstantin Matyash, Alexander V. Khrabrov, Rod W. Boswell, and Amnon Fruchtman. Physics of $\mathbf{E} \times \mathbf{B}$ discharges relevant to plasma propulsion and similar technologies. *Physics of Plasmas*, 27(12):120601, 2020.
- ²Jean-Pierre Boeuf and Andrei Smolyakov. Physics and instabilities of low-temperature $\mathbf{E} \times \mathbf{B}$ plasmas for spacecraft propulsion and other applications. *Physics of Plasmas*, 30(5):050901, 2023.
- ³A. I. Smolyakov, O. Chapurin, W. Frias, O. Koshkarov, I. Romadanov, T. Tang, M. Uman-sky, Y. Raitses, I. D. Kaganovich, and V. P. Lakhin. Fluid theory and simulations of instabilities, turbulent transport and coherent structures in partially-magnetized plasmas of $\mathbf{E} \times \mathbf{B}$ discharges. *Plasma Physics and Controlled Fusion*, 59(1):014041, 2017.
- ⁴S. N. Abolmasov. Physics and engineering of crossed-field discharge devices. *Plasma Sources Science & Technology*, 21(3):035006, 2012.
- ⁵Y. Sakawa, C. Joshi, P. K. Kaw, F. F. Chen, and V. K. Jain. Excitation of the modified Simon-Hoh instability in an electron-beam produced plasma. *Physics of Fluids B-Plasma Physics*, 5(6):1681–1694, 1993.
- ⁶Y. Sakawa, C. Joshi, P. K. Kaw, V. K. Jain, T. W. Johnston, F. F. Chen, and J. M. Dawson. Nonlinear evolution of the modified Simon-Hoh instability via a cascade of side-band instabilities in a weak beam-plasma system. *Physical Review Letters*, 69(1):85–88, 1992.
- ⁷E. Rodriguez, V. Skoutnev, Y. Raitses, A. Powis, I. Kaganovich, and A. Smolyakov. Boundary-induced effect on the spoke-like activity in $\mathbf{E} \times \mathbf{B}$ plasma. *Physics of Plas-*

- mas*, 26(5):053503, 2019.
- ⁸C. L. Ellison, Y. Raitses, and N. J. Fisch. Cross-field electron transport induced by a rotating spoke in a cylindrical Hall thruster. *Physics of Plasmas*, 19(1):013503, 2012.
- ⁹M. S. McDonald and A. D. Gallimore. Rotating spoke instabilities in Hall thrusters. *IEEE Transactions on Plasma Science*, 39(11):2952–2953, 2011.
- ¹⁰A. Hecimovic, V. Schulz-von der Gathen, M. Boke, A. von Keudell, and J. Winter. Spoke transitions in HiPIMS discharges. *Plasma Sources Science & Technology*, 24(4):045005, 2015.
- ¹¹RC Przybocki and MA Cappelli. Coherent high-frequency axial oscillations in a partially magnetized direct current magnetron discharge. *Physical Review Letters*, 132(22):225301, 2024.
- ¹²M. Lee, C. Cheon, J. Choi, H. J. Lee, Y. S. Hwang, K. J. Chung, and J. Y. Kim. Azimuthal and axial dispersion relations of low-frequency oscillations in partially magnetized plasma with crossed electric and magnetic fields. *Physics of Plasmas*, 30(10):103502, 2023.
- ¹³Cheongbin Cheon, Jinyoung Choi, John Bon-Woong Koo, and June Young Kim. Experimental evidence of various mode numbers of azimuthal waves in an penning source for semiconductor processing. *Plasma Sources Science and Technology*, 32(7):07LT01, 2023.
- ¹⁴J. Carlsson, I. Kaganovich, A. Powis, Y. Raitses, I. Romadanov, and A. Smolyakov. Particle-in-cell simulations of anomalous transport in a Penning discharge. *Physics of Plasmas*, 25(6):061201, 2018.
- ¹⁵A. T. Powis, J. A. Carlsson, I. D. Kaganovich, Y. Raitses, and A. Smolyakov. Scaling of spoke rotation frequency within a Penning discharge. *Physics of Plasmas*, 25(7):072110, 2018.
- ¹⁶Liang Xu, Denis Eremin, and Ralf Peter Brinkmann. Direct evidence of gradient drift instability being the origin of a rotating spoke in a crossed field plasma. *Plasma Sources Science and Technology*, 30(7):075013, 2021.
- ¹⁷Jean-Pierre Boeuf. Rotating structures in low-temperature magnetized plasmas—insight from particle simulations. *Frontiers in Physics*, 2:74, 2014.
- ¹⁸K. Matyash, R. Schneider, S. Mazouffre, S. Tsikata, and L. Grimaud. Rotating spoke instabilities in a wall-less Hall thruster: Simulations. *Plasma Sources Science and Technology*, 28(4):044002, 2019.

- ¹⁹J. L. Vay, A. Almgren, J. Bell, L. Ge, D. P. Grote, M. Hogan, O. Kononenko, R. Lehe, A. Myers, C. Ng, J. Park, R. Ryne, O. Shapoval, M. Thévenet, and W. Zhang. Warp-x: A new exascale computing platform for beam–plasma simulations. *Nuclear Instruments and Methods in Physics Research Section A: Accelerators, Spectrometers, Detectors and Associated Equipment*, 909:476–479, 2018.
- ²⁰M. Tyushev, M. Papahn Zadeh, V. Sharma, M. Sengupta, Y. Raitses, J.-P. Boeuf, and A. Smolyakov. Azimuthal structures and turbulent transport in penning discharge. *Physics of Plasmas*, 30(3):033506, 2023.
- ²¹Nirbhav Singh Chopra, Ivan Romadanov, and Yevgeny Raitses. Production of warm ions in electron beam generated $\mathbf{E} \times \mathbf{B}$ plasma. *Applied Physics Letters*, 124:064101, 2024.
- ²²O Zatsarinny and K Bartschat. B-spline breit–pauli r-matrix calculations for electron collisions with argon atoms. *Journal of Physics B: Atomic, Molecular and Optical Physics*, 37(23):4693, 2004.
- ²³C Yamabe, SJ Buckman, and AV Phelps. Measurement of free-free emission from low-energy-electron collisions with ar. *Physical Review A*, 27(3):1345, 1983.
- ²⁴Marie-Claude Bordage, SF Biagi, LL Alves, K Bartschat, S Chowdhury, Leanne C Pitchford, GJM Hagelaar, WL Morgan, V Puech, and O Zatsarinny. Comparisons of sets of electron–neutral scattering cross sections and swarm parameters in noble gases: Iii. krypton and xenon. *Journal of Physics D: Applied Physics*, 46(33):334003, 2013.
- ²⁵L. Brieda. Plasma simulations by example. 2019.
- ²⁶C.K. Birdsall and A.B. Langdon. *Plasma Physics Via Computer Simulation*. Adam Hilger series on plasma physics. McGraw-Hill, 1985.
- ²⁷R. Lucken, A. Bourdon, M. A. Lieberman, and P. Chabert. Instability-enhanced transport in low temperature magnetized plasma. *Physics of Plasmas*, 26(7):070702, 2019.
- ²⁸C. N. Lashmore-Davies. Negative energy waves. *Journal of Plasma Physics*, 71:101–109, 2005.
- ²⁹O. Koshkarov, A. I. Smolyakov, A. Kapulkin, Y. Raitses, and I. Kaganovich. Nonlinear structures of lower-hybrid waves driven by the ion beam. *Physics of Plasmas*, 25(6):61209, 2018.
- ³⁰O. Koshkarov, A. I. Smolyakov, I. V. Romadanov, O. Chapurin, M. V. Umansky, Y. Raitses, and I. D. Kaganovich. Current flow instability and nonlinear structures in dissipative two-fluid plasmas. *Physics of Plasmas*, 25(1):011604, 2018.

- ³¹R. Gueroult, J. M. Rax, and N. J. Fisch. Centrifugal instability in the regime of fast rotation. *Physics of Plasmas*, 24(8):082102, 2017.
- ³²S. Aggarwal, Y. Camenen, A. Escarguel, and A. Poyé. Centrifugal instability in a weakly magnetized rotating plasma column. *Journal of Plasma Physics*, 89(3), 2023.
- ³³G. Fubiani, Garrigue L., F. Gaboriau, A. Smolyakov, and Y. Camenen. 3D PIC/MCC modeling of the dynamics of rotating spokes in a penning discharge. *77th Annual Gaseous Electronics Conference*, page 082102, Sep 30–Oct 4, 2024; San Diego, CA 2024.
- ³⁴A. T. Powis and I. D. Kaganovich. Accuracy of the explicit energy-conserving particle-in-cell method for under-resolved simulations of capacitively coupled plasma discharges. *Physics of Plasmas*, 31(2):023901, 2024.
- ³⁵D. C. Barnes and L. Chacón. Finite spatial-grid effects in energy-conserving particle-in-cell algorithms. *Computer Physics Communications*, 258:107560, 2021.
- ³⁶Monson H Hayes. *Statistical digital signal processing and modeling*. John Wiley & Sons, 2009.
- ³⁷J. P. Boeuf. Ionization waves (striations) in a low-current plasma column revisited with kinetic and fluid models. *Physics of Plasmas*, 29(2):022105, 2022.
- ³⁸N. Brenning. Review of the CIV phenomenon. *SPACE SCIENCE REVIEWS*, 59(3-4):209–314, 1992.
- ³⁹June Young Kim, Jinyoung Choi, Jaeyoung Choi, Y. S. Hwang, and Kyoung-Jae Chung. Efficiency improvement of an $\mathbf{E} \times \mathbf{B}$ penning discharge source by enhanced cross-field transport of electrons. *Plasma Sources Science and Technology*, 31(5):05LT02, 2022.
- ⁴⁰G. Fubiani, G. J. M. Hagelaar, J. P. Boeuf, and S. Kolev. Modeling a high power fusion plasma reactor-type ion source: Applicability of particle methods. *Physics of Plasmas*, 19(4):043506, 2012.
- ⁴¹J. P. Boeuf, J. Claustre, B. Chaudhury, and G. Fubiani. Physics of a magnetic filter for negative ion sources. II. $\mathbf{E} \times \mathbf{B}$ drift through the filter in a real geometry. *Physics of Plasmas*, 19(11):113510, 2012.
- ⁴²J. P. Boeuf. Micro instabilities and rotating spokes in the near-anode region of partially magnetized plasmas. *Physics of Plasmas*, 26(7):072113, 2019.
- ⁴³M. Panjan and A. Anders. Plasma potential of a moving ionization zone in dc magnetron sputtering. *Journal of Applied Physics*, 121(6):063302, 2017.

- ⁴⁴S. Gallian, W. N. G. Hitchon, D. Eremin, T. Mussenbrock, and R. P. Brinkmann. A phenomenological model for the description of rotating spokes in hipims discharges. *Plasma Sources Science & Technology*, 22(5):055012, 2013.
- ⁴⁵J. P. Boeuf and M. Takahashi. New insights into the physics of rotating spokes in partially magnetized $\mathbf{E} \times \mathbf{B}$ plasmas. *Physics of Plasmas*, 27(8):083520, 2020.